Applying machine learning to improve the near-real-time products of the Aura Microwave Limb Sounder

Frank Werner[1], Nathaniel J. Livesey[1], Luis F. Millán[1], William G. Read[1], Michael J. Schwartz[1],
Paul A. Wagner[1], William H. Daffer[1], Alyn Lambert[1], Sasha N. Tolstoff[2], and Michelle L. Santee[1]

[1]Jet Propulsion Laboratory, California Institute of Technology, 4800 Oak Grove Drive, Pasadena, CA 91109, USA
[2]California Institute of Technology, 1200 East California Blvd, Pasadena, CA 91105, USA

Correspondence: Frank Werner (frank.werner@jpl.nasa.gov)

Abstract. A new algorithm to derive near-real-time (NRT) data products for the Aura Microwave Limb Sounder (MLS) is presented. The old approach was based on a simplified optimal estimation retrieval algorithm (OE-NRT) to reduce computational demands and latency. This manuscript describes the setup, training, and evaluation of a redesigned approach based on artificial neural networks (ANN-NRT), which is trained on > 17 years of MLS radiance observations and composition profile

5   retrievals. Comparisons of joint histograms and performance metrics derived between the two NRT results and the operational MLS products demonstrate a noticeable statistical improvement from ANN-NRT. This new approach results in higher correlation coefficients, as well as lower root-mean-square deviations and biases at almost all retrieval levels compared to OE-NRT. The exceptions are pressure levels with concentrations close to $0\,\mathrm{ppbv}$, where the ANN models tend to underfit and predict zero. Depending on the application, this behavior might be advantageous. While the developed models can take advantage of

10   the extended MLS data record, this study demonstrates that training ANN-NRT on just a single year of MLS observations is sufficient to improve upon OE-NRT. This confirms the potential of applying machine learning to the NRT efforts of other current and future mission concepts.

1 Introduction

15   The Aura Microwave Limb Sounder (MLS) data record is more than 18 years long, far exceeding the MLS 5-year design life. Due to its exceptionally long duration and reliability (e.g., Hubert et al., 2016; Hegglin et al., 2021; Read et al., 2022), MLS observations are employed to study a wide range of atmospheric science topics, such as long-term trends in atmospheric constituents (e.g., Gaudel et al., 2018; Lossow et al., 2018; Strahan and Douglass, 2018; Froidevaux et al., 2019), global troposphere-stratosphere transport (e.g., Neu et al., 2014; Diallo et al., 2019), the influence of strong convective systems on

20   lower-stratospheric humidity (e.g., Schwartz et al., 2013; Werner et al., 2020), as well as the impact of wildfires and volcanic eruptions on stratospheric chemistry (e.g., Pumphrey et al., 2015; Schwartz et al., 2020; Millán et al., 2022; Santee et al., 2022), to name just a few.

Processing of the standard retrieval products provided by MLS takes a little less than a full day and thus cannot be used in near-real-time (NRT) applications. Therefore, the MLS team started providing NRT data based on a simplified retrieval algo-
25 rithm for a limited selection of its standard species in 2008. These products are routinely produced within 3 hours of the MLS observations (Lambert et al., 2022) and can thus be delivered to the scientific community much more expeditiously. Examples of MLS NRT usage are the assimilation of MLS NRT ozone (O_3) profiles into the Copernicus Atmosphere Monitoring Service (CAMS) from the European Centre for Medium-Range Weather Forecasts (ECMWF) (e.g., Peuch et al., 2022), as well as deliveries of O_3, water vapor (H_2O), and carbon monoxide (CO) maps over Southeast Asia during the Asian Summer Mon-
30 soon Chemical & Climate Impact Project (ACCLIP; https://www.eol.ucar.edu/field_projects/acclip/, last access: 19 December 2022) campaign in 2022 (Pan et al., 2022). MLS NRT O_3 and temperature (T) profiles are also assimilated by the numerical weather prediction model of the Naval Research Laboratory (Hoppel et al., 2008), while NRT H_2O and sulphur dioxide (SO_2) are part of the NASA Major Volcanic Eruption Response Plan (NASA, 2018). While MLS NRT data help to constrain the model forecasts, monitor the stratopshere during volcanic eruptions, and aid flight planning during aircraft campaigns, they are
35 less reliable than the standard MLS products and require careful screening procedures (Lambert et al., 2022).

Recent years have seen a proliferation of the application of machine learning approaches in atmospheric sciences, from dimensionality reduction of satellite observations (e.g., Del Frate et al., 2005), to estimates of aerosol particle loading (e.g., Grivas and Chaloulakou, 2006) and cloud cover (e.g., Saponaro et al., 2013; Werner et al., 2020), to land cover studies (e.g., Campos-Taberner et al., 2020), to weather and climate modelling (e.g., Schultz et al., 2021). Two of the main benefits of ap-
40 plying machine learning techniques to answer atmospheric science questions are (i) pattern recognition enabling identification of previously unknown or poorly understood relationships between observations and the atmospheric state and (ii) the increase in computational efficiency leading to faster turnaround times in predicting the atmospheric variable of interest.

In this study we describe an updated Aura MLS NRT setup that applies artificial neural networks (ANN) to facilitate faster and more reliable predictions of MLS NRT constituent profiles. This new algorithm provides both of the above mentioned
45 benefits of machine learning techniques: (i) it pinpoints the relevant MLS radiance observations that reliably determine the individual species profiles and (ii) yields NRT profile predictions an order of magnitude faster than the previous algorithm it replaces. The manuscript is structured as follows: an introduction to MLS observations, retrieved data products, and retrieval algorithms is given in section 2. An overview of the ANN setup, training, and evaluation is presented in section 3. A comparison of the former and updated NRT algorithm encompassing joint histograms, performance metrics, and global maps is given in
50 section 4. The main conclusions and a brief summary are presented in section 6.

2 Data

Aura MLS has observed brightness temperatures from five spectral frequency ranges centered around 118, 190, 240, 640, and 2,500 GHz since 2004 (Waters et al., 2006). The 2,500 GHz band targeted the hydroxyl radical; it was deactivated in 2010 and is not considered here. Table 4 in Waters et al. (2006) and Figure 2.1.1 in Livesey et al. (2022) give an overview and additional
55 details on individual MLS bands and channels as well as the specific absorption characteristics of the various atmospheric

constituents that are targeted. Daily MLS observations comprise ≈ 3500 vertical limb scans (called major frames; MAFs), each of which takes $\approx 20\,\mathrm{s}$ to complete. Each MAF consists of 125 radiance integrations (called minor frames; MIFs) during a continuous vertical scan of the limb. In this study, MLS brightness temperatures sampled over 2005–2022 are used as the input variables (commonly called "features") for each of the trained ANN models.

60 MLS brightness temperatures provide the means for the profile retrievals of various atmospheric properties and trace gas concentrations. Here, retrieved profiles of temperature (T), as well as concentrations of H_2O, O_3, CO, SO_2, nitric acid (HNO_3), and nitrous oxide (N_2O) provide the output variables (commonly called "labels") for each ANN model. The MLS level 2 (L2) Geophysical Product files report the respective operational profile retrievals; we use the most recent data, version 5 (Livesey et al., 2022). The spatial resolution of the L2 products depends on the species of interest, but typical values are $3\,\mathrm{km}$ in the

65 vertical and 5 and $500\,\mathrm{km}$ in the cross-track and along-track dimensions, respectively. The along-track distance between adjacent profiles is $\approx 165\,\mathrm{km}$. Only valid data, following the detailed data screening rules provided in Livesey et al. (2022), are considered. Information on the species-specific time range considered for training the ANN, as well as the employed MLS bands, channels, and MIFs used as input for the ANNs, are summarized in Table 1.

Results of the ANN algorithm are also compared to those of the previous NRT retrievals based on optimal estimation (OE-

70 NRT) (Lambert et al., 2022). The OE-NRT retrievals are based on a modified L2 algorithm, which is necessary to reduce the data and computational resources. This imposes a number of limitations on the NRT products, such as a reduced number of valid profile retrievals and limitations on the recommended pressure ranges. Individual screening rules and recommendations are provided in Lambert et al. (2022); note that the OE-NRT data product already employs the T-ANN presented in this study.

3 Artificial neural network

75 ### 3.1 Theory and general setup

A feedforward ANN is a type of machine learning model that consists of sequential layers that contain a large number of connected neurons, where the information only gets propagated forward from layer to layer. Propagating information backwards is not permitted. A more in-depth description of ANN setups and the involved mathematics can be found in, e.g., Reed and Marks (1999), Goodfellow et al. (2016), and Werner et al. (2021). Similar to the latter study, the model setup and determination of

80 model weights are facilitated by the "Keras" library for Python (version 2.2.4; Chollet et al., 2015), with "TensorFlow" (version 1.13.1) as the backend (Abadi et al., 2016).

A simplified sketch of the general model setup is shown in Figure 1. Note that the actual setup for each individual ANN-NRT model is notably more complex. The input layer, shown in blue, contains an $m \times n$ matrix of n features sampled at m different times and/or locations. In this study, the features are n MLS brightness temperatures from individual spectral bands,

85 channels, and MIFs from m different MAFs (see Table 1 for the model-specific details). An example of a single MAF of MLS band 2 radiances is illustrated in Figure 1; the transition from black to white colors indicates the profiles sampled in channels 1–25. Each feature in the input layer is connected to individual neurons in the first hidden layer ($N_{1,n}$, $n = 1, 2, \cdots, n$), shown in green. Each neuron value is derived as a linear superposition of the weighted input features. A subsequent activation layer
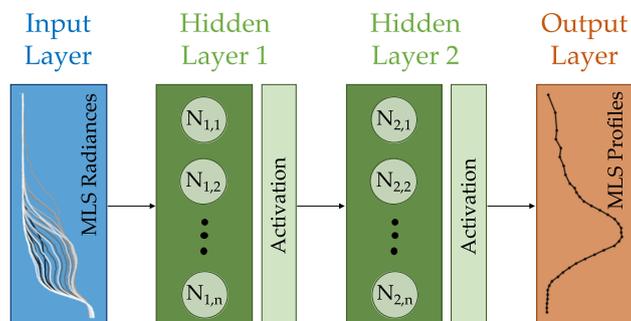
Figure 1. Simplified sketch of the algorithm setup.

introduces a degree of non-linearity. The simplified model in Figure 1 consists of a second hidden layer that contains neurons
$N_{2,n}$, n $= 1, 2, \cdots, n$. Here, each neuron value is calculated as a linear superposition of the weighted neuron output of the first
hidden layer, after it passed through the first activation layer. Finally, following a second activation layer, there is the output
layer (shown in dark orange), which consists of an $m \times k$ matrix of k different labels. Here, the labels are values from individual
profiles of a specific MLS retrieved L2 atmospheric constituent. An example of a single O_3 profile is shown in Figure 1. As
before, each neuron $N_{2,n}$ in the second hidden layer is connected to each of the k labels by means of individual weights.

A detailed description of the training procedure is given in Werner et al. (2021). The necessary steps include randomly
splitting the complete data set into training, validation, and test data ($75, 20, 5\%$ for each model in this study), determining
the optimal hyperparameters via k-fold cross-validation, and the final training and validation of the model with the best set of
hyperparameters. The hyperparameters that were considered in each model setup, some of which are described in more detail
below, are (i) the number of hidden layers (n_{HL}), (ii) the number of neurons per hidden layer (n_N), (iii) the activation function
(AF) employed in the activation layer, (iv) the amount of regularization, either via weight decay (i.e., the L2 regularization
parameter; LRP) or alternatively the standard deviation of an extra Gaussian noise layer (GNS), and (v) the mini-batch size
(MBS). The variables n_{HL} and n_N determine the complexity of the model. The choice of AF specifies the non-linear mathe-
matical transformation of the individual neuron output. Introducing an LRP is one method to introduce regularization during
the ANN training, which usually improves generalization of the model predictions for previously unseen data. Another method
is to add Gaussian noise to each neuron input; the standard deviation of the noise added directly impacts the level of regulariza-
tion. During the training process the model weights are determined by iteratively minimizing a pre-defined loss function (the
root-mean-square error, RMSE, in this study). Instead of using the full training data set during each iteration, only a random
subset of the training data is used, determined by the parameter MBS. This approach not only improves generalization of the
models (due to the introduced noise when minimizing the loss function), but also speeds up the training process.

Three additional hyperparameters that are not listed here are the choice of optimizer that minimizes the loss function during
training; the learning rate, which affects the speed of convergence during training; and the number of "epochs", which is
the number of iterations during training. We found that "Adam" optimization with a learning rate of 10^{-5} yielded the best
model performance for each of the NRT species. Each model was trained with $\approx 10,000$ epochs, and the lowest validation loss

115 was recorded. The ideal model weights are those associated with the minimum validation loss. Additional information about hyperparameters and their impact on model performance is given in, e.g., Reed and Marks (1999) and Goodfellow et al. (2016).

3.2 Hyperparameters and performance metrics for each model

Table 1 gives an overview of the ideal hyperparameters for each NRT species, determined after a comprehensive training procedure. It also provides details on the features that make up the input matrix for each ANN-NRT model, namely the start and end dates that define the training data record for each model, and the respective MLS bands, channels, and MIFs. Note that

120 the MIFs for all models basically cover the vertical range of $\approx 400 - 0.001\,\text{hPa}$. Since the models for each of the target species were developed separately, the end dates for the employed training data vary slightly. The choice of bands and channels was based on the absorption characteristics of each target molecule, as well as possible interference of other species.

Note that the model setups for CO and SO_2 differ from those of the other species. MLS mid-stratospheric observations of CO are basically just noise, which negatively affected model performance in the upper troposphere/lower stratosphere (UTLS)

125 and in the upper stratosphere/mesosphere, where CO signals are stronger. The CO NRT product is of particular interest in the UTLS. As a result, we decided to train two different CO models: one for the four MLS retrieval levels in the UTLS between 215 and $68\,\text{hPa}$, and a second one for all other levels (including noisy levels in the middle stratosphere). The final CO profile predictions are a combination of both models.

Similarly, MLS SO_2 retrievals at all stratospheric levels can be considered noise under standard atmospheric conditions.

130 Elevated values are observed in air masses perturbed by volcanic eruptions. As a result, the SO_2 model was developed with a reduced data set covering periods of volcanic activity, namely the eruptions of Kasatochi, Calbuco, Sarychev, Nabro, Raikoke, and Hunga Tonga-Hunga Ha'apai (e.g., Pumphrey et al., 2015; Millán et al., 2022).

The hyperparameters reported in Table 1 are the ANN-NRT settings associated with the models that exhibited the highest performance scores during the training process. These scores were derived by comparing the ANN-NRT predictions with the

135 respective MLS L2 results for all MAFs in the independent test data set. Three specific scores were considered: Pearson's product-moment correlation coefficient (R), the root-mean-square deviation (RMSD) normalized by the average L2 value, and the median of the relative deviation between the derived ANN-NRT prediction and the L2 product (i.e., the relative bias). Additional comparisons of R, RMSD, and the bias from the test data set to those calculated from the training and validation data sets were performed to ensure that the model performance for previously unseen data is comparable to that for the data

140 involved in the training process.

The performance metrics derived for the independent test data set for each of the different ANN-NRT models are presented in Table 2. Since each of the MLS constituents describes a profile retrieval, the average over all valid retrieval levels is reported. With the exception of the SO_2 predictions, the average R and biases are > 0.71 and $< 1.1\%$, respectively. The ANN models designed to predict T, H_2O, and O_3 perform particularly well, with $R > 0.88$ and RMSD$< 12\%$. As mentioned in section 2,

145 stratospheric L2 retrievals in the absence of elevated levels of SO_2 can be considered noise, and comparisons between L2 and ANN-NRT results are difficult ($R < 0.26$ and bias $> 7\%$). However, ANN-NRT performance metrics for enhanced concentrations due to the Hunga Tonga-Hunga Ha'apai volcanic eruption are shown in Figure A1–B1. The associated ANN-NRT

Table 1. Summary of input features and hyperparameters for each ANN model. See text for more details.

	Data Record	Bands	Channels	MIFs	n_{HL}	n_N	AF	LRP	GNS	MBS
T	01/01/2005–05/31/2021	1 8 22	1–25 1–25 40–90	23–97	2	5,078	relu	n/a	10^{-1}	8,192
H_2O	01/01/2005–03/31/2022	1 2 3 23	1–25 1–25 1–25 40–90	23–126	2	400	tanh	5^{-4}	n/a	32
O_3	01/01/2005–04/30/2022	1 7 8 24	1–25 1–25 1–25 40–90	23–126	2	5,078	relu	n/a	10^{-1}	32
CO-UTLS	01/01/2005–04/30/2022	8 9	1–25 1–22	23–56	2	1,068	tanh	n/a	n/a	32
CO	01/01/2005–04/30/2022	1 8 9 25	1–25 1–25 1–22 40–90	23–126	2	800	tanh	n/a	n/a	32
SO_2	08/07/2008–09/02/2008 04/23/2015–05/07/2015 06/14/2009–07/19/2009 06/13/2011–06/28/2011 06/22/2019–08/18/2019 01/14/2022–01/28/2022	8	1–25	23–126	2	1,739	relu	n/a	10^{-1}	32
HNO_3	01/01/2005–08/31/2022	1 4 6 33	1–25 1–25 1–25 1–4	23–126	2	400	tanh	5^{-4}	n/a	32
N_2O	01/01/2005–08/31/2022	1 3 8	1–25	23–126	2	400	tanh	5^{-4}	n/a	32

Table 2. Summary of performance metrics for an independent test data set for each of the ANN-NRT models, namely the average correlation coefficient (R), the average root-mean-square deviation (RMSD), and the average bias. Both the RMSD and bias are normalized by the average L2 value at each level. Averages are calculated over all valid pressure levels.

	R	RMSD (%)	Bias (%)
T	0.95	0.88	0.011
H_2O	0.89	11.08	-1.10
O_3	0.94	10.83	-0.01
CO-UTLS	0.72	24.43	-0.08
CO	0.74	68.21	-0.25
SO_2	0.26	-206.99	7.26
HNO_3	0.75	-6.42	0.06
N_2O	0.89	93.03	-0.03

predictions exhibit significantly higher (lower) R (RMSD, biases) compared to the estimates from OE-NRT at all retrieval levels.

4 Results

4.1 Statistical comparison with MLS L2

Figure 2a and Figure 2c show joint histograms of the OE-NRT and L2 T retrievals at $21.54\,\mathrm{hPa}$ (in the middle stratosphere) and $100.00\,\mathrm{hPa}$ (in the UTLS). Data are from MLS observations over 1–31 July 2021, a period not employed in the ANN-NRT training process. Similar comparisons between the ANN-NRT predictions and L2 retrievals are shown in Figure 2b and d. Not only are the ANN-NRT distributions narrower at both of the levels shown, but also there are fewer outliers far away from the 1:1 line. Compared to the OE-NRT results, the ANN-NRT predictions exhibit higher correlation coefficients ($R = 0.98, 0.99$ vs. $R = 0.99, 1.00$ for 100.00 and $21.54\,\mathrm{hPa}$, respectively) and a smaller range of minimum/maximum deviations from the L2 results.

Similar joint histograms for H_2O are shown in Figure 2e-h. Because this ANN-NRT model was trained well after the T model and the training data includes MLS observations sampled as late as April 2022, the comparisons shown here are for 1–31 May 2022. This provides the means to (i) assess ANN-NRT performance for previously unseen data and (ii) evaluate the ability of ANN-NRT to reproduce the unprecedented H_2O enhancements in the persistent Hunga Tonga-Hunga Ha'apai plume (e.g., Millán et al., 2022). The H_2O distribution at $21.54\,\mathrm{hPa}$ reveals a significant underestimation in the OE-NRT retrievals for
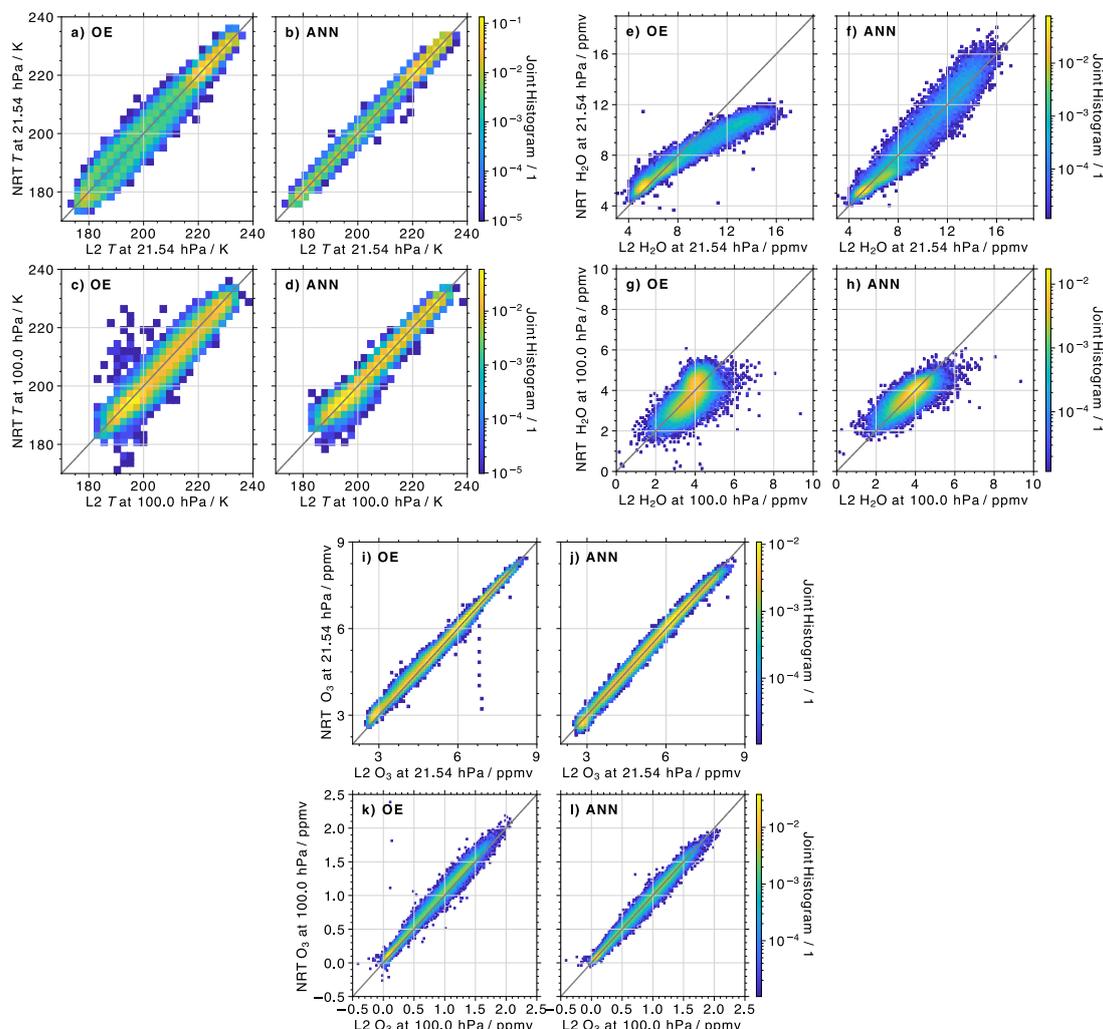
Figure 2. (a) Joint histograms of T derived from OE-NRT and L2 at $21.54\,\mathrm{hPa}$. Data are from MLS observations over 1–31 July 2021. The gray diagonal line indicates 1:1 correlation. (b) Similar to (a), but showing joint histograms of the ANN-NRT and L2 results. (c)-(d) Same as (a)-(b), but at $100.00\,\mathrm{hPa}$. (e)-(h) and (i)-(l) Similar to (a)-(d), but for H_2O and O_3 over 1–31 May 2022.

profiles with $H_2O > 8\,\mathrm{ppmv}$ associated with the volcanic plume. In contrast, the ANN-NRT can reliably predict values of up to

165    $16\,\mathrm{ppmv}$. At $100.00\,\mathrm{hPa}$, the ANN-NRT distribution is noticeably narrower, with fewer outliers off the 1:1 line compared to the OE-NRT results. At the $100\,\mathrm{hPa}$ pressure level, the ANN-NRT predictions have a significantly higher correlation coefficient than the OE-NRT retrievals ($R = 0.80$ compared to $R = 0.66$), while the 1st and 99th percentile of the differences with L2 are reduced ($0.9\,\mathrm{ppmv}$ compared to $1.3\,\mathrm{ppmv}$). At the $21.54\,\mathrm{hPa}$ level both NRT products exhibit $R = 0.98$.

Comparisons of L2, OE-NRT, and ANN-NRT O_3 are shown in panels (i)-(l). The OE-NRT algorithm performs well at

170   both levels, with $R = 1.00$ and only a few obvious outliers observed, while ANN-NRT provides similarly good performance
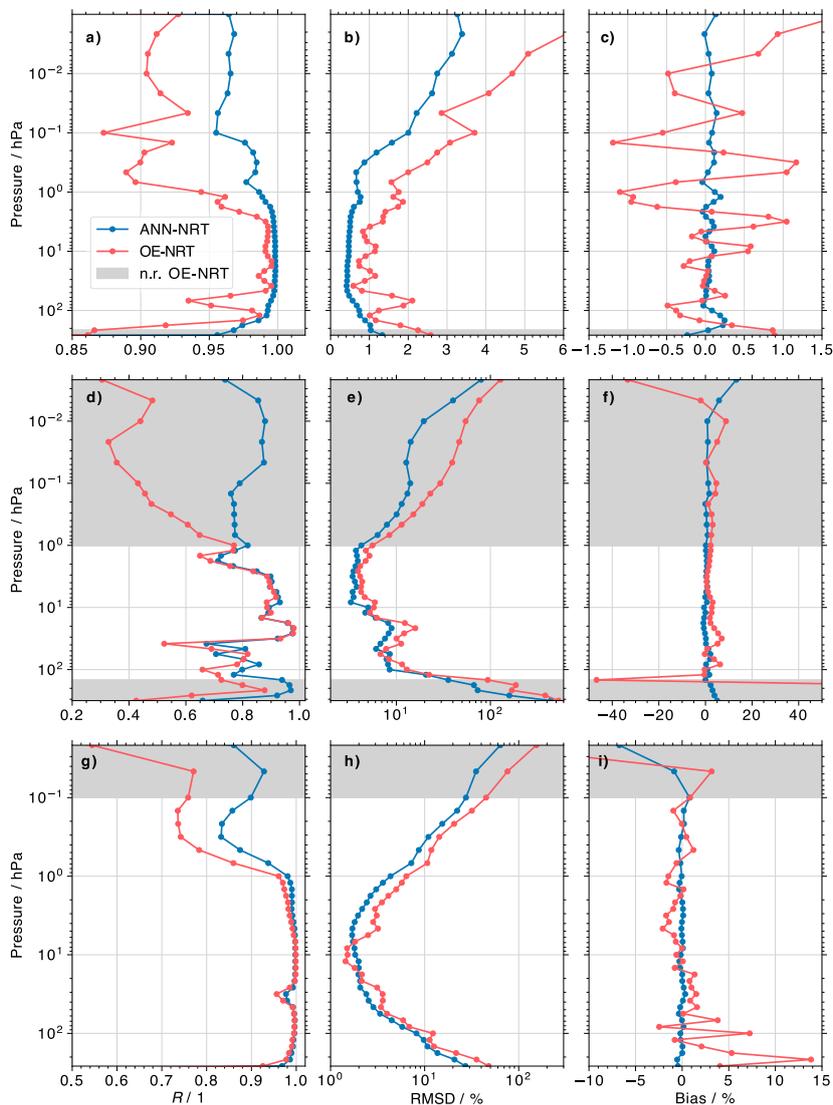
Figure 3. (a) Profiles of correlation coefficient (R) between OE-NRT and L2 T (red), as well as the ANN-NRT and L2 results (blue). Data are from MLS observations over 1–31 July 2021. The vertical extent is defined by the recommended L2 data screening procedures; gray areas indicate levels at which the OE-NRT product is not recommended for scientific use. (b)-(c) Same as (a), but showing the root-mean-square deviation (RMSD) and bias, respectively. Both the RMSD and bias are normalized by the average L2 T at each level. (d)-(f) and (g)-(i) Similar to (a)-(c), but for H_2O and O_3, respectively, over 1–31 May 2022.

($R = 1.00$ at both levels). Joint histograms between L2 retrievals and the OE-NRT results, as well as the ANN-NRT predictions for CO, SO_2, HNO_3, and N_2O, are shown in Figure A1 in the appendix.

Table 3. Summary of average correlation coefficient (R), average absolute root-mean-square deviation (RMSD), and average absolute bias, as well as the averages of the 1st and 99th percentile of the difference between the various OE-NRT and L2 products, and the ANN-NRT and L2 results. The RMSD, bias, and percentile differences are normalized by the average L2 value at each level. Averages are calculated over all valid OE-NRT pressure levels.

	R		RMSD (%)		Bias (%)		1st perc. (%)		99th perc. (%)	
	OE	ANN	OE	ANN	OE	ANN	OE	ANN	OE	ANN
T	0.95	0.99	2.00	1.01	0.50	0.07	-4.94	-2.43	4.72	2.44
H_2O	0.82	0.85	11.03	7.21	3.99	0.61	-26.77	-19.20	26.42	19.47
O_3	0.95	0.97	9.93	6.79	1.79	0.18	-21.04	-16.95	23.56	16.40
CO-UTLS	0.68	0.78	37.18	27.83	12.07	1.18	-72.60	-64.04	84.39	65.25
CO	0.79	0.75	62.19	58.52	12.922	7.59	-148.00	-156.18	139.53	134.42
SO_2	0.26	0.56	923.39	610.92	115.73	9.16	355.89	289.23	-244.61	-238.91
HNO_3	0.73	0.72	49.38	39.12	6.19	13.17	-119.60	-105.40	110.05	53.57
N_2O	0.96	0.94	46.92	44.84	34.33	1.83	-76.91	-102.82	58.44	105.66

Figure 3 presents profiles of three metrics that characterize the performance of the two NRT algorithms. Panels (a)-(c) show derived R, RMSD, and bias between T from L2 and OE-NRT (red), as well as between L2 and ANN-NRT (blue). At all retrieval levels, the ANN-based T predictions have higher R (> 0.950) and lower RMSD ($< 3.4\%$). The ANN-NRT bias shows little vertical variability and is within $\pm 0.3\%$ at all levels, whereas the OE-NRT bias shows some oscillatory behavior and much larger variability (values within $\pm 1.5\%$).

The recommended range for the OE-NRT H_2O retrievals is 147–1 hPa. Here, the performance metrics for the ANN-NRT predictions compare well to those of the OE-NRT retrievals, and the derived R, RMSD, and bias values are very similar (panels (d)-(f)). Outside of that range the OE-NRT performance degrades noticeably and ANN-NRT yields more reliable H_2O values that are closer to the L2 retrievals. Here R is > 0.75, RMSD is $< 65\%$, and the bias is within 15%. In the case of the O_3 retrievals (panels (g)-(j)), the derived R values for the OE-NRT and ANN-NRT algorithms are very similar. Only above ≈ 1 hPa does the OE-NRT performance suffer, and the correlations between the L2 and the ANN-NRT results are more than 0.1 higher. At almost all retrieval levels, the ANN-NRT exhibits slightly smaller RMSD and biases compared to the OE-NRT algorithm. Similar profiles for CO, SO_2, HNO_3, and N_2O are shown in Figure A2 in the appendix.

A summary of the average R, average absolute RMSD, and average absolute bias for each species and the two NRT algorithms, as well as the averages of the 1st and 99th percentile of the differences to L2 (as a proxy for the minimum and maximum deviations), are given in Table 3. Averages are calculated over all valid pressure ranges (excluding levels not recommended for OE-NRT). Note that the SO_2 statistics are based on MLS observations in January 2022, which are affected by the Hunga

190 Tonga-Hunga Ha'apai volcanic eruption and were included in training data set. Except for the stratospheric CO, N_2O, and HNO_3 models, the ANN-NRT predictions always exhibit higher R, lower RMSD, lower biases, and lower minimum and maximum differences to L2. These three species are sampled at a number of stratospheric levels where the retrieved concentrations are very close to zero and can be considered noise. As illustrated in Figures A1 and A2, the OE-NRT algorithm fits that noise better than the ANN-NRT models. Apart from the noisy retrieval levels, the ANN-NRT approach provides profile predictions

195 that agree better with the operational MLS L2 data products.

4.2 Global maps for individual example days

Figure 4a presents global maps of temperatures provided by the operational MLS L2 algorithm (left column), the OE-NRT product (middle column), and the ANN-NRT predictions (right column). Data are from 12 July 2021, a representative example day that was not part of the training data set and thus unseen by the ANN-NRT model. Each temperature product is shown

200 at two different levels: at $100.00\,hPa$ in the UTLS (bottom panels) and at $21.54\,hPa$ in the middle stratosphere (top panels). At both levels the three data products provide similar results, and both the OE-NRT and ANN-NRT algorithm reproduce the general patterns observed in the L2 temperatures. Compared to the L2 results, the OE-NRT product exhibits an increased frequency of invalid retrievals, as reflected by the areas in white over the Southern Ocean.

Similar example maps for H_2O and O_3 on 22 May 2022 are shown in Figure 4b and 4c. At $100.00\,hPa$ there are areas

205 with strong overestimates of the H_2O from OE-NRT compared to L2 (dark blue colors), while concentrations in the tropics and subtropics are generally underestimated (light violet colors). Here, the ANN-NRT performs more reliably, and the results are closer to the L2 data. At this level the OE-NRT algorithm also yields slight overestimates of tropical O_3, indicated by the lighter blue colors. In the middle stratosphere at $21.54\,hPa$, the significant underestimates of tropical H_2O from the OE-NRT retrievals is evident, which confirms the results seen in Figure 2e. The ANN-NRT algorithm is able to replicate the elevated L2

210 concentrations. At this level the O_3 concentrations from the two NRT approaches are very similar. The only obvious difference is the area of low concentrations over Antarctica, which is completely missed by the OE-NRT algorithm and overestimated (in area) by ANN-NRT. Similar maps for CO, SO_2, HNO_3, and N_2O are shown in Figure B1 in the appendix.

5 ANN-NRT performance for different amounts of training data

The analysis in section 4 illustrates that the new ANN-NRT algorithm generally provides reliable results in closer agreement

215 to the operational MLS L2 products (compared to OE-NRT). This shows that it is possible, potentially advisable, to employ machine learning techniques to obtain more reliable NRT data products for current and future mission concepts. However, the good performance of ANN-NRT may hinge on the long MLS data record, which encompasses more than 17 years of global observations. If ANN-based NRT approaches only provide reliable results when trained on extensive data sets that only become available after many years of observations, then machine learning might be a less attractive solution after all. In order to

220 test how the amount of available training data affects the reliability of the ANN-NRT predictions, we calculated performance metrics for two of the ANN-NRT models in this study when trained with differently sized training data sets. Note that the
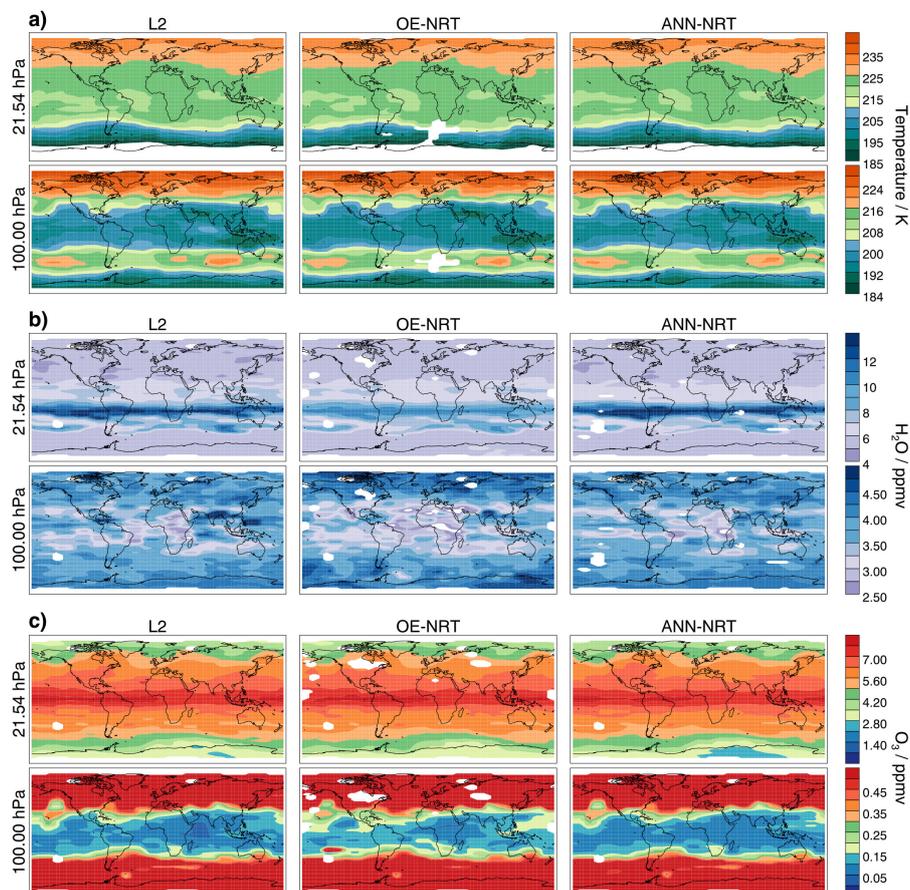
Figure 4. (a) Maps of derived T provided by the MLS L2, OE-NRT, and ANN-NRT algorithm at two different levels on 12 July 2021. (b)-(c) Similar to (a), but for H_2O and O_3, respectively, on 22 May 2022.

training data size refers to all data involved in the training and evaluation procedure and thus also includes the validation and test data set. For the analysis in this section, the size of the training data was first set to one year, and subsequently doubled to two, four, and eight years. The performance metrics derived for each of these models were then compared to the ones for the fully trained ANN-NRT algorithm, i.e., using the data records indicated in Table 1. We focus on the models for T and O_3, i.e., quantities for which the OE-NRT algorithms perform comparatively poorly and well, respectively.

Figure 5 shows the average R, RMSD, and bias between the operational MLS L2 retrievals and both the OE-NRT and ANN-NRT results for the two species. Similar to the analysis in Figures 2 and 3, the comparisons are based on observations over 1–31 July 2021 (T) and 1–31 May 2022 (O_3). Averages (red lines and blue dots for OE-NRT and ANN-NRT, respectively) and standard deviations (blue error bars; for clarity only shown for the ANN-NRT predictions) are calculated over all valid pressure levels following the data screening procedures for the OE-NRT products, thus ignoring levels in the extended ANN-NRT range indicated in section 4.1. It is obvious that for both species, average R values increase monotonically with increasing training
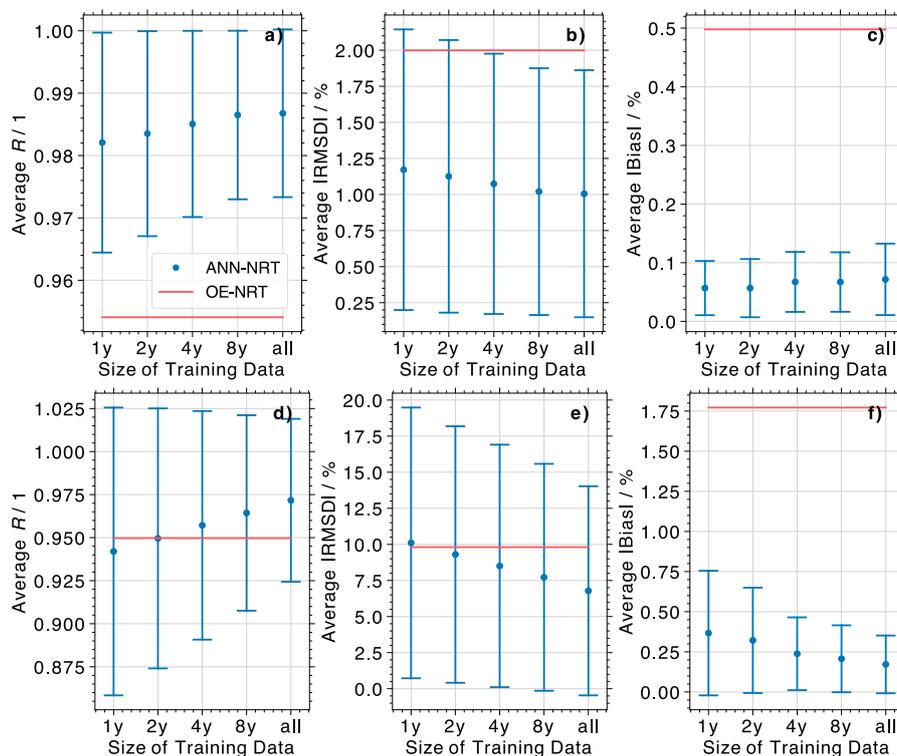
Figure 5. (a) Average correlation coefficient (R) between T from the MLS L2 and OE-NRT retrieval algorithms (red line), as well as the L2 and ANN-NRT results (blue dots), for differently sized training data sets. Vertical bars indicate the range covered by ± 1 standard deviation, based on the variability in R for different retrieval levels. (b)-(c) Same as (a), but showing the average absolute root-mean-square deviation (RMSD) and bias. Both the RMSD and bias are normalized by the average L2 temperature at each level. (d)-(f) Similar to (a)-(c), but for ozone.

data size, while the average RMSD monotonically decreases. At the same time, the standard deviation for each metric slightly decreases. A very small increase in the absolute bias is observed.

235   Surprisingly, even if just a single year of observations is available to train the ANN-NRT T model, the derived performance metrics show a significant improvement when compared with the OE-NRT results. Here, R increases from 0.95 to 0.98, the RMSD is reduced from 2.00% to 1.17%, and the absolute bias is reduced from 0.50% to 0.06%. Even for O_3, where the current NRT algorithm performs rather well, the ANN model trained on one year of MLS observations yields noticeable improvements. While the correlation coefficients and RMSD are comparable (0.95 vs. 0.94 and 9.93% vs. 10.10%), the absolute bias is reduced

240   from 1.79% to 0.37%.

    These results illustrate that the simplified OE-NRT retrieval algorithm could have been replaced by machine learning approaches as early as one year after the beginning of the mission, which would have resulted in more reliable NRT data products.

6 Conclusions

The previous version of MLS NRT data products (OE-NRT, Lambert et al., 2022) replaced the originally OE-based temperature
(T) retrieval with predictions from an artificial neural network (ANN). This manuscript not only demonstrates the improved
reliability of the machine learning approach, it also describes the setup and evaluation of ANN models for all other NRT
species. Starting in January 2023, all MLS NRT data products are based on this new approach (ANN-NRT).

The biggest improvements compared to OE-NRT are observed for T, water vapor (H_2O), and O_3. The analysis in this study
shows that for these products the ANN-NRT algorithm yields noticeably higher correlation coefficients (R), as well as lower
root-mean-square deviations (RMSD) and biases when compared to the operational L2 results.

The ANN-NRT predictions for carbon monoxide (CO), nitric acid (HNO_3), and nitrous oxide (N_2O) are characterized
by good performance at most retrieval levels. However, the OE-NRT algorithm does a better job at fitting the L2 noise for
concentrations close to 0 ppbv. Here, ANN-NRT tends towards predicting 0 ppbv regardless of the L2 values, which might be
the preferable behavior as it produces less noisy background concentrations.

Of special note is the ANN-NRT setup for sulphur dioxide (SO_2). Volcanic eruptions are the primary source of stratospheric
SO_2. As a result, we decided to train the SO_2 ANN model on MLS observations around major volcanic eruptions, namely those
of Kasatochi, Calbuco, Sarychev, Nabro, Raikoke, and Hunga Tonga-Hunga Ha'apai (e.g., Pumphrey et al., 2015; Millán et al.,
2022). While ANN-NRT performs well in reproducing elevated SO_2 concentrations associated with the Hunga Tonga-Hunga
Ha'apai eruption, the training data is limited and the model might suffer from overfitting (i.e., learning specific characteristics
of known eruptions well to the detriment of generalization).

Besides the better agreement with the operational L2 retrievals (compared to OE-NRT), the ANN-NRT approach is compu-
tationally more efficient. Current tests reveal that ANN-NRT provides data $\approx 5 - 12$ times faster than the OE-NRT algorithm.

The results presented in this manuscript indicate that, instead of relying on simplified retrieval algorithms and assumed
approximations to provide timely NRT data products, machine learning approaches can be utilized to obtain results both more
reliably and more rapidly. However, the application to MLS data benefits from the extended data record of more than 17 years
of daily, global observations. A sensitivity study was performed to test the effects of significantly reduced amounts of training
data on the reliability of predicted T and O_3. ANN-NRT models were trained with 1, 2, 4, and 8 years of MLS observations,
and the performance in each case was compared to results from the best models, which were trained on > 17 years of data.
This simulates the process of training the ANN-NRT setup after 1, 2, 4, and 8 years of observations. It is shown that even
models that were trained on only one year of MLS data outperform the OE-NRT algorithm, which demonstrates the potential
of applying machine learning to generate NRT products for other current and future mission concepts.

Data availability. MLS L1 radiance data and L2GP data, including status flags, are available at https://disc.gsfc.nasa.gov. NRT data are
available at https://www.earthdata.nasa.gov/learn/find-data/near-real-time/mls.
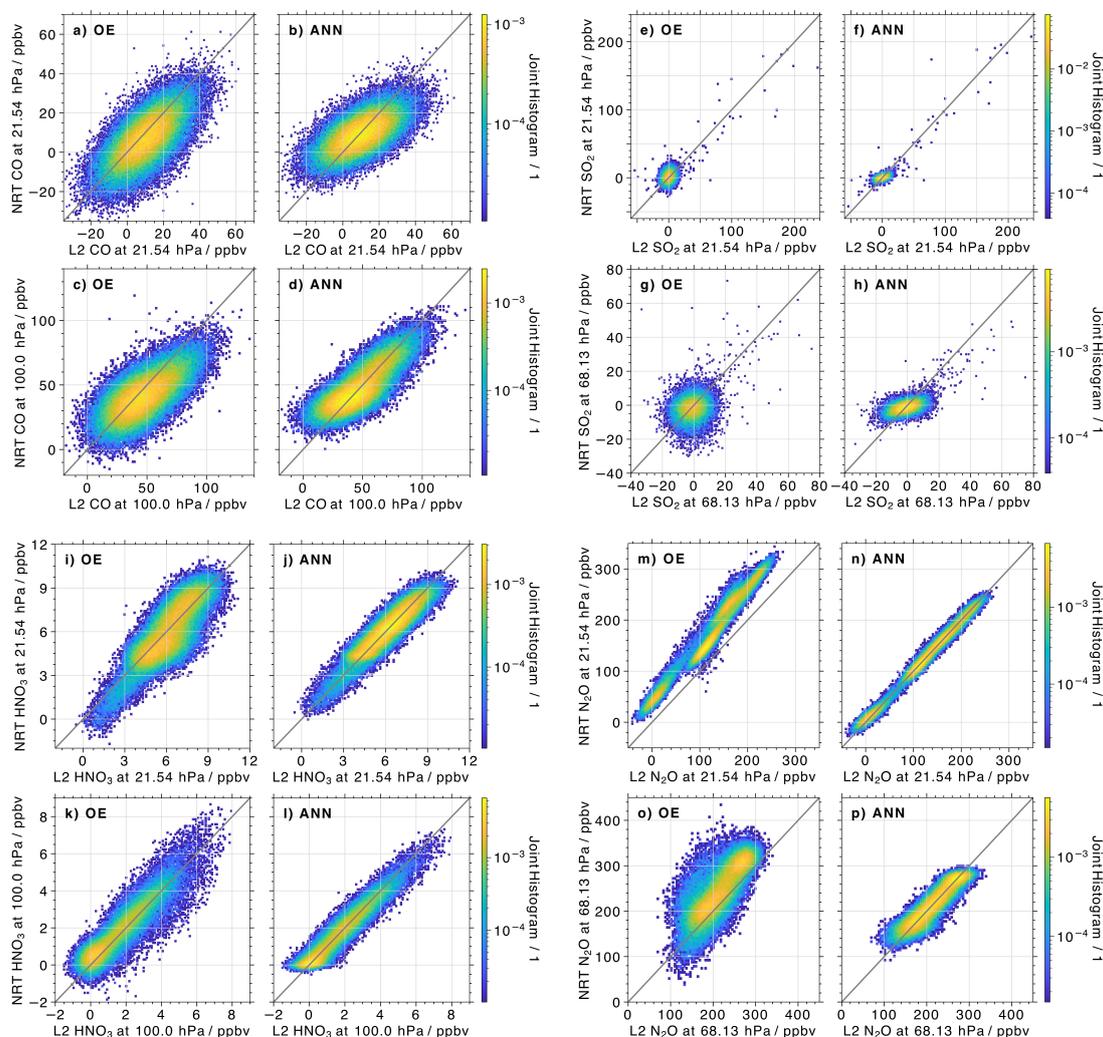
Figure A1. Similar to Fig.2, but for (a)-(d) CO over 1–31 May 2022, (e)-(h) SO$_2$ over 15–22 January 2022, as well as (i)-(l) HNO$_3$ and (m)-(p) N$_2$O over 1–30 September 2022.

Appendix A: Statistical comparison with MLS L2: CO, SO$_2$, HNO$_3$, and N$_2$O

This section presents joint histograms (Figure A1) and profiles of performance metrics (Figure A2) derived for the CO, SO$_2$, HNO$_3$, and N$_2$O retrievals from the three algorithms. These results complete the analysis described in section 4.1.

There are no CO sources in the middle stratosphere, and the MLS retrievals can be primarily considered noise. This is evident in Figure A1a, which shows a joint histogram of L2 and OE-NRT retrievals at 21.54 hPa. The distribution is centered around very low positive values, and almost all retrievals are in the range -20 to 40 ppbv. A similar distribution of L2 and ANN-NRT results is shown in panel (b), albeit with a slight tilt relative to the 1:1 line. The ANN-NRT $R = 0.51$ is slightly

lower than the one for OE-NRT ($R = 0.55$). Noticeably higher CO concentrations are observed at $100.00\,\mathrm{hPa}$; the respective joint histograms are shown in Figure A1c-d. Here, the ANN-NRT distribution shows values closer to the 1:1 line compared to the OE-NRT results, which indicates a higher correlation between the predictions and L2 retrievals ($R = 0.80$ vs. $R = 0.68$).

As mentioned in sections 2–4, background SO_2 concentrations in the stratosphere are essentially $0\,\mathrm{ppbv}$ and the MLS
285 retrievals can be considered noise. However, air masses that are affected by volcanic eruptions show significantly enhanced concentrations. The joint histograms of L2 and OE-NRT, as well as L2 and ANN-NRT results, are shown in Figure A1e-h. Data are from 15–22 January 2022, the first week after the Hunga Tonga-Hunga Ha'apai eruption (e.g., Millán et al., 2022). Each distribution is centered around concentrations of $0\,\mathrm{ppbv}$, but individual MLS profiles show elevated concentrations of up to $200\,\mathrm{ppbv}$ (at $21.54\,\mathrm{hPa}$) and $80\,\mathrm{ppbv}$ (at $68.13\,\mathrm{hPa}$; this level was chosen to present profiles that are less affected by the
290 volcanic eruption). The parts of the ANN-NRT distributions that resemble SO_2 noise are tighter and appear almost horizontal, indicating that the ANN-NRT tends to predict concentrations close to $0\,\mathrm{ppmv}$ independent of the L2 noise. Conversely, the distributions from the L2 and OE-NRT results appear random for the noisy part and slightly more scattered around the 1:1 line for observations in the volcanic plume. Correlation coefficients are higher for the ANN-NRT results, both in the middle stratosphere ($R = 0.86$ vs. $R = 0.70$) and in the UTLS ($R = 0.62$ vs. $R = 0.46$).

295 Figure A1i-l shows a clear improvement for the HNO_3 predictions based on the ANN-NRT model compared to the OE-NRT algorithm. The distributions are tighter, and fewer outliers are noticeable at both the 21.54 ($R = 0.92$ vs. $R = 0.83$) and $100.00\,\mathrm{hPa}$ ($R = 0.96$ vs. $R = 0.92$) levels. A similarly stark improvement from the ANN-NRT algorithm is evident for N_2O, indicated by the joint histograms in Figure A1m-p. Not only does ANN-NRT remove the noticeable bias that is evident in the OE-NRT results, but also the distributions are closer to the 1:1 line ($R = 0.99/R = 0.92$ vs. $R = 0.98/R = 0.81$ at
300 $68.13/21.54\,\mathrm{hPa}$). Note that MLS N_2O retrievals are not recommended at $100.00\,\mathrm{hPa}$.

Similar to earlier analysis, Figure A2 provides a more quantitative evaluation of the OE-NRT and ANN-NRT performance. Again, profiles of derived performance metrics from the MLS L2 products and the current OE- and ANN-based NRT results are presented.

While the ANN-NRT CO predictions exhibit slightly higher (lower) R (RMSD) values in the UTLS and upper stratosphere,
305 the ANN-NRT approach seems to do worse in the middle stratosphere between ≈ 46 and $3.2\,\mathrm{hPa}$. At these levels, the CO retrievals can be considered noise, where the ANN-NRT tends to predict values closer to $0\,\mathrm{ppbv}$ regardless of the L2 value. Meanwhile, the ANN-NRT bias varies within 15% and shows fewer oscillations than the OE-NRT results.

The ANN-NRT performance metrics for SO_2 indicate a more reliable SO_2 prediction than from the OE-NRT algorithm, with better R, RMSD, and bias results at every retrieval level. This can be partly explained by the fact that 75% of MLS
310 profiles sampled over 1–22 January 2022 are included in the training data set for the ANN-NRT model in order to focus on model reliability for air masses affected by volcanic eruptions. Predicting concentrations for observations over 1–31 May 2022 provides the means to evaluate ANN-NRT performance for previously unseen data, albeit for a time period without SO_2 enhancements due to volcanic influence. Compared to the OE-NRT results, the ANN-NRT predictions are characterized by higher R, as well as lower RMSD and biases, at all valid retrieval levels. As an example, the ANN-NRT algorithm (OE-NRT)
315 exhibits $R = 0.34$ ($R = 0.22$) at $21.54\,\mathrm{hPa}$ and $R = 0.22$ ($R = 0.14$) at $68.13\,\mathrm{hPa}$.
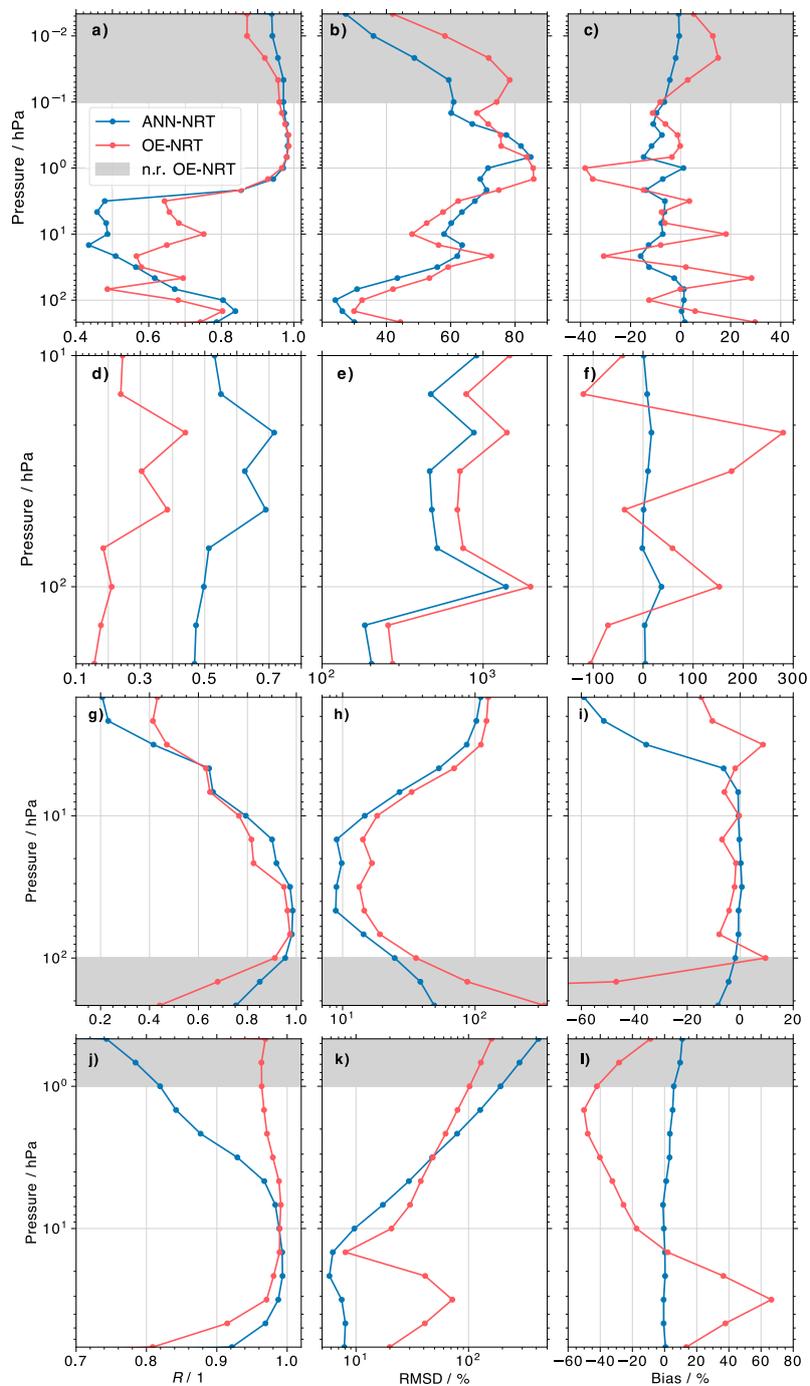
Figure A2. Similar to Fig.3, but showing performance metrics for (a)-(c) CO over 1–31 May 2022, (d)-(f) SO$_2$ over 15–22 January 2022, as well as (g)-(i) HNO$_3$ and (j)-(l) N$_2$O over 1–30 September 2022.

Apart from retrieval levels above $\approx 4.6\,\text{hPa}$, the HNO_3 predictions from ANN-NRT compare better with the MLS L2 retrievals, indicated by higher R, as well as lower RMSD and bias values. This improvement is especially noticeable in the upper troposphere (pressures $> 100\,\text{hPa}$), where the OE-NRT product is not recommended.

Similar to CO, there are pressure levels where the N_2O retrievals can be considered noise (in the upper stratosphere for pressures below $\approx 5\,\text{hPa}$). Here, the ANN-NRT results exhibit lower R and higher RMSD. However, the bias remains small, with values within $\approx 10\%$.

Appendix B: Global maps for individual example days: CO, SO$_2$, HNO$_3$, and N$_2$O

This section presents global maps of CO, SO_2, HNO_3, and N_2O from the three algorithms for representative example days (Figure B1) and completes the analysis in section 4.2.

Figure B1a shows CO on 22 May 2022 from the L2, OE-NRT, and ANN-NRT algorithms at $100.00\,\text{hPa}$ (bottom panels) and $21.54\,\text{hPa}$. Two characteristics that were previously mentioned are noticeable: ANN-NRT outperforms the OE-NRT algorithm in the UTLS (see the enhanced concentrations in the region of the Asian summer monsoon; red colors), while it predicts smoother CO noise with concentrations closer to $0\,\text{ppbv}$ (see the absence of red colors in the Northern Hemisphere at $21.54\,\text{hPa}$). Similar observations about the performance for noisy data can be made for the SO_2 example map, shown in Figure B1b. At both retrieval levels, ANN-NRT reproduces the enhanced values in Indian Ocean (at $68.13\,\text{hPa}$) and over the African continent (at $21.54\,\text{hPa}$), while predicted concentrations everywhere else are closer to $0\,\text{ppbv}$ (light gray and light salmon colors).

Differences between the OE-NRT and ANN-NRT algorithms are more subtle for the HNO_3 field, presented in Figure B1c. In the tropics and subtropics at $100.00\,\text{hPa}$, the OE-NRT concentrations are slightly too low (compared to L2), as indicated by the darker purple colors. Similar underestimations in the OE-NRT retrievals are noticeable at $21.54\,\text{hPa}$, especially in the Southern Ocean west of South America and over Antarctica.

Significant differences are observed for the global N_2O fields in Figure B1d. The OE-NRT retrievals exhibit strong over-estimation (dark red colors) in the tropics, subtropics, and mid-latitudes. Likewise, concentrations in the polar regions are too high (dark purple colors). The ANN-NRT approach not only does a much better job at reproducing the L2 retrievals, but it also does not suffer from the data gaps (white colors) apparent in the L2 data, which arise from the extensive screening rules..
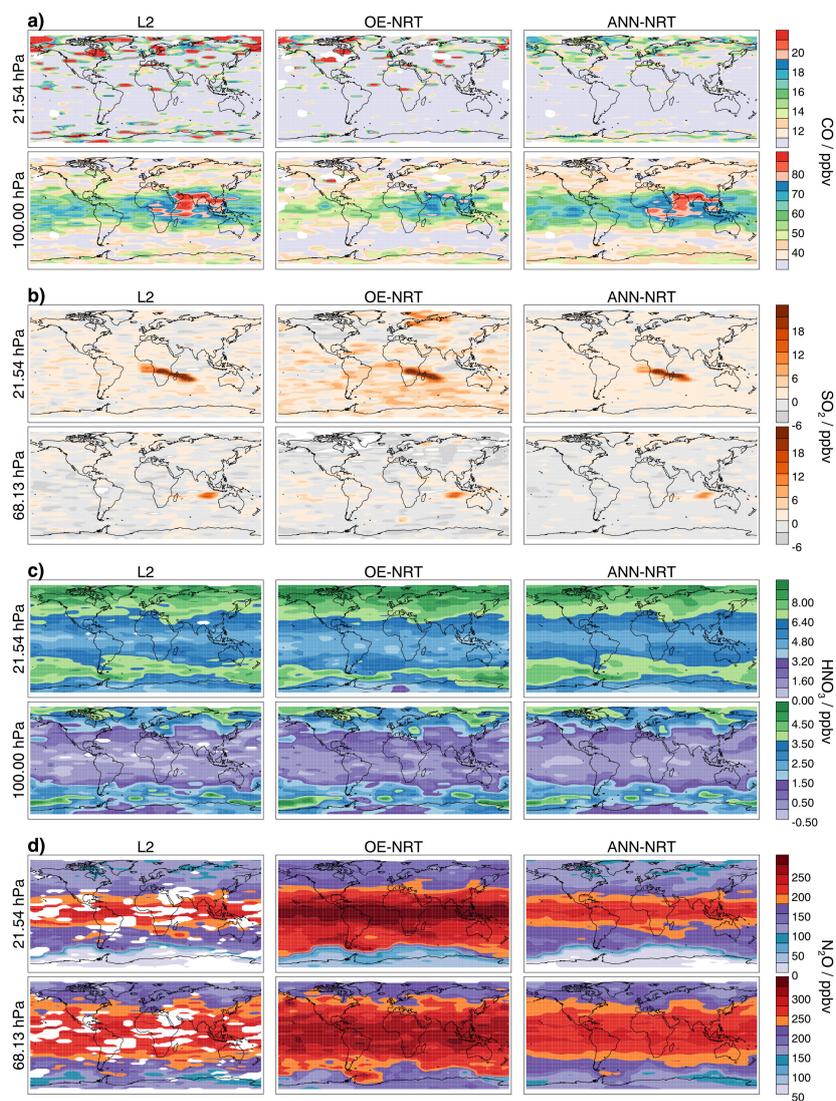
Figure B1. Similar to Fig.4, but showing maps of (a) CO on 22 May 2022, (b) SO$_2$ on 22 January 2022, as well as (c) HNO$_3$ and (d) N$_2$O on 22 September 2022.

Author contributions. FW, NJL, LFM, WGR, MJS, AL, and MLS have shaped the concept of this study and refined the approach during extensive discussions. FW, PAW, and WHD implemented the ANN approach into the current NRT algorithm chain. FW, LFM, and SNT carried out the data analysis and prepared the figures for the manuscript. FW wrote the initial draft of the manuscript, which was subsequently refined by all authors.

345   *Competing interests.* The authors declare that they have no conflict of interest.

Acknowledgements. ©2023. California Institute of Technology. Government sponsorship acknowledged. The research was carried out at the Jet Propulsion Laboratory, California Institute of Technology, under a contract with the National Aeronautics and Space Administration (80NM0018D0004).

References

350   Abadi, M., Agarwal, A., Barham, P., Brevdo, E., Chen, Z., Citro, C., Corrado, G. S., Davis, A., Dean, J., Devin, M., Ghemawat, S., Good-fellow, I., Harp, A., Irving, G., Isard, M., Jia, Y., Jozefowicz, R., Kaiser, L., Kudlur, M., Levenberg, J., Mane, D., Monga, R., Moore, S., Murray, D., Olah, C., Schuster, M., Shlens, J., Steiner, B., Sutskever, I., Talwar, K., Tucker, P., Vanhoucke, V., Vasudevan, V., Viegas, F., Vinyals, O., Warden, P., Wattenberg, M., Wicke, M., Yu, Y., and Zheng, X.: TensorFlow: Large-Scale Machine Learning on Heterogeneous Distributed Systems, arXiv [preprint], arxiv:1603.04467v2, 2016.

355   Campos-Taberner, M., García-Haro, F. J., Martínez, B., Izquierdo-Verdiguier, E., Atzberger, C., Camps-Valls, G., and Gilabert, M. A.: Understanding deep learning in land use classification based on Sentinel-2 time series, Scientific Reports, 10, 17 188, https://doi.org/10.1038/s41598-020-74215-5, 2020.

Chollet, F. et al.: Keras, https://keras.io, 2015.

Del Frate, F., Iapaolo, M., Casadio, S., Godin-Beekmann, S., and Petitdidier, M.: Neural networks for the dimensionality reduction of
360   GOME measurement vector in the estimation of ozone profiles, Journal of Quantitative Spectroscopy and Radiative Transfer, 92, 275–291, https://doi.org/10.1016/j.jqsrt.2004.07.028, 2005.

Diallo, M., Konopka, P., Santee, M. L., Müller, R., Tao, M., Walker, K. A., Legras, B., Riese, M., Ern, M., and Ploeger, F.: Structural changes in the shallow and transition branch of the Brewer–Dobson circulation induced by El Niño, Atmospheric Chemistry and Physics, 19, 425–446, https://doi.org/10.5194/acp-19-425-2019, 2019.

365   Froidevaux, L., Kinnison, D. E., Wang, R., Anderson, J., and Fuller, R. A.: Evaluation of CESM1 (WACCM) free-running and specified dynamics atmospheric composition simulations using global multispecies satellite data records, Atmospheric Chemistry and Physics, 19, 4783–4821, https://doi.org/10.5194/acp-19-4783-2019, 2019.

Gaudel, A., Cooper, O. R., Ancellet, G., Barret, B., Boynard, A., Burrows, J. P., Clerbaux, C., Coheur, P.-F., Cuesta, J., Cuevas, E., Doniki, S., Dufour, G., Ebojie, F., Foret, G., Garcia, O., Granados-Muñoz, M. J., Hannigan, J. W., Hase, F., Hassler, B., Huang, G., Hurtmans,
370   D., Jaffe, D., Jones, N., Kalabokas, P., Kerridge, B., Kulawik, S., Latter, B., Leblanc, T., Le Flochmoën, E., Lin, W., Liu, J., Liu, X., Mahieu, E., McClure-Begley, A., Neu, J. L., Osman, M., Palm, M., Petetin, H., Petropavlovskikh, I., Querel, R., Rahpoe, N., Rozanov, A., Schultz, M. G., Schwab, J., Siddans, R., Smale, D., Steinbacher, M., Tanimoto, H., Tarasick, D. W., Thouret, V., Thompson, A. M., Trickl, T., Weatherhead, E., Wespes, C., Worden, H. M., Vigouroux, C., Xu, X., Zeng, G., and Ziemke, J.: Tropospheric Ozone Assessment Report: Present-day distribution and trends of tropospheric ozone relevant to climate and global atmospheric chemistry model evaluation,
375   Elementa: Science of the Anthropocene, 6, https://doi.org/10.1525/elementa.291, 39, 2018.

Goodfellow, I., Bengio, Y., and Courville, A.: Deep Learning (Adaptive Computation and Machine Learning series), The MIT Press, Cambridge, MA, 2016.

Grivas, G. and Chaloulakou, A.: Artificial neural network models for prediction of PM10 hourly concentrations, in the Greater Area of Athens, Greece, Atmospheric Environment, 40, 1216–1229, https://doi.org/10.1016/j.atmosenv.2005.10.036, 2006.

380   Hegglin, M. I., Tegtmeier, S., Anderson, J., Bourassa, A. E., Brohede, S., Degenstein, D., Froidevaux, L., Funke, B., Gille, J., Kasai, Y., Kyrölä, E. T., Lumpe, J., Murtagh, D., Neu, J. L., Pérot, K., Remsberg, E. E., Rozanov, A., Toohey, M., Urban, J., von Clarmann, T., Walker, K. A., Wang, H.-J., Arosio, C., Damadeo, R., Fuller, R. A., Lingenfelser, G., McLinden, C., Pendlebury, D., Roth, C., Ryan, N. J., Sioris, C., Smith, L., and Weigel, K.: Overview and update of the SPARC Data Initiative: comparison of stratospheric composition measurements from satellite limb sounders, Earth System Science Data, 13, 1855–1903, https://doi.org/10.5194/essd-13-1855-2021, 2021.

385   Hoppel, K. W., Baker, N. L., Coy, L., Eckermann, S. D., McCormack, J. P., Nedoluha, G. E., and Siskind, D. E.: Assimilation of stratospheric
         and mesospheric temperatures from MLS and SABER into a global NWP model, Atmospheric Chemistry and Physics, 8, 6103–6116,
         https://doi.org/10.5194/acp-8-6103-2008, 2008.

        Hubert, D., Lambert, J.-C., Verhoelst, T., Granville, J., Keppens, A., Baray, J.-L., Bourassa, A. E., Cortesi, U., Degenstein, D. A., Froidevaux,
         L., Godin-Beekmann, S., Hoppel, K. W., Johnson, B. J., Kyrölä, E., Leblanc, T., Lichtenberg, G., Marchand, M., McElroy, C. T., Murtagh,
390   D., Nakane, H., Portafaix, T., Querel, R., Russell III, J. M., Salvador, J., Smit, H. G. J., Stebel, K., Steinbrecht, W., Strawbridge, K. B.,
         Stübi, R., Swart, D. P. J., Taha, G., Tarasick, D. W., Thompson, A. M., Urban, J., van Gijsel, J. A. E., Van Malderen, R., von der Gathen, P.,
         Walker, K. A., Wolfram, E., and Zawodny, J. M.: Ground-based assessment of the bias and long-term stability of 14 limb and occultation
         ozone profile data records, Atmospheric Measurement Techniques, 9, 2497–2534, https://doi.org/10.5194/amt-9-2497-2016, 2016.

        Lambert, A., Read, W. G., Froidevaux, L., Schwartz, M. J., Werner, F., Wagner, P. A., Daffer, W. H., Livesey, N. J., Pumphrey, H. C., Manney,
395   G. L., Santee, M. L., Valle, L. F. M., Knosp, B., Vuu, C., and Gluck, S.: Version 5 Level-2 Near-Real-Time Data User Guide., Tech. Rep.
         JPL D-48439 c, Jet Propulsion Laboratory, California Institute of Technology, Pasadena, California, 91109-8099, 2022.

        Livesey, N. J., Read, W. G., Wagner, P. A., Froidevaux, L., Santee, M. L., Schwartz, M. J., Lambert, A., Valle, L. F. M., Pumphrey, H. C.,
         Manney, G. L., Fuller, R. A., Jarnot, R. F., Knosp, B. W., and Lay, R. R.: Version 5.0x Level 2 and 3 data quality T S and description
         document., Tech. Rep. JPL D-105336 Rev. B, Jet Propulsion Laboratory, California Institute of Technology, Pasadena, California, 91109-
400   8099, 2022.

        Lossow, S., Hurst, D. F., Rosenlof, K. H., Stiller, G. P., von Clarmann, T., Brinkop, S., Dameris, M., Jöckel, P., Kinnison, D. E., Plieninger,
         J., Plummer, D. A., Ploeger, F., Read, W. G., Remsberg, E. E., Russell, J. M., and Tao, M.: Trend differences in lower stratospheric
         water vapour between Boulder and the zonal mean and their role in understanding fundamental observational discrepancies, Atmospheric
         Chemistry and Physics, 18, 8331–8351, https://doi.org/10.5194/acp-18-8331-2018, 2018.

405   Millán, L., Santee, M. L., Lambert, A., Livesey, N. J., Werner, F., Schwartz, M. J., Pumphrey, H. C., Manney, G. L., Wang, Y., Su, H., Wu,
         L., Read, W. G., and Froidevaux, L.: The Hunga Tonga-Hunga Ha'apai Hydration of the Stratosphere, Geophysical Research Letters, 49,
         e2022GL099 381, https://doi.org/10.1029/2022GL099381, 2022.

        NASA: NASA Major Volcanic Eruption Response Plan, vol. version 11, Greenbelt, https://acd-ext.gsfc.nasa.gov/Documents/NASA_reports/
         Docs/VolcanoWorkshopReport_v12.pdf, 2018.

410   Neu, J. L., Flury, T., Manney, G. L., Santee, M. L., Livesey, N. J., and Worden, J.: Tropospheric ozone variations governed by changes in
         stratospheric circulation, Nature Geoscience, 7, 340–344, https://doi.org/10.1038/ngeo2138, 2014.

        Pan, L. L., Kinnison, D., Liang, Q., Chin, M., Santee, M. L., Flemming, J., Smith, W. P., Honomichl, S. B., Bresch, J. F., Lait, L. R., Zhu, Y.,
         Tilmes, S., Colarco, P. R., Warner, J., Vuvan, A., Clerbaux, C., Atlas, E. L., Newman, P. A., Thornberry, T., Randel, W. J., and Toon, O. B.:
         A Multimodel Investigation of Asian Summer Monsoon UTLS Transport Over the Western Pacific, Journal of Geophysical Research:
415   Atmospheres, 127, e2022JD037 511, https://doi.org/10.1029/2022JD037511, 2022.

        Peuch, V.-H., Engelen, R., Rixen, M., Dee, D., Flemming, J., Suttie, M., Ades, M., Agustí-Panareda, A., Ananasso, C., Andersson, E.,
         Armstrong, D., Barré, J., Bousserez, N., Dominguez, J. J., Garrigues, S., Inness, A., Jones, L., Kipling, Z., Letertre-Danczak, J., Par-
         rington, M., Razinger, M., Ribas, R., Vermoote, S., Yang, X., Simmons, A., de Marcilla, J. G., and Thépaut, J.-N.: The Copernicus
         Atmosphere Monitoring Service: From Research to Operations, Bulletin of the American Meteorological Society, 103, E2650 – E2668,
420   https://doi.org/10.1175/BAMS-D-21-0314.1, 2022.

        Pumphrey, H. C., Read, W. G., Livesey, N. J., and Yang, K.: Observations of volcanic SO$_2$ from MLS on Aura, Atmospheric Measurement
         Techniques, 8, 195–209, https://doi.org/10.5194/amt-8-195-2015, 2015.

Read, W. G., Stiller, G., Lossow, S., Kiefer, M., Khosrawi, F., Hurst, D., Vömel, H., Rosenlof, K., Dinelli, B. M., Raspollini, P., Nedoluha, G. E., Gille, J. C., Kasai, Y., Eriksson, P., Sioris, C. E., Walker, K. A., Weigel, K., Burrows, J. P., and Rozanov, A.: The SPARC Water
425   Vapor Assessment II: assessment of satellite measurements of upper tropospheric humidity, Atmospheric Measurement Techniques, 15, 3377–3400, https://doi.org/10.5194/amt-15-3377-2022, 2022.

Reed, R. and Marks, ll, R. J.: Neural Smithing: Supervised Learning in Feedforward Artificial Neural Networks, A Bradford Book, 1999.

Santee, M. L., Lambert, A., Manney, G. L., Livesey, N. J., Froidevaux, L., Neu, J. L., Schwartz, M. J., Millán, L. F., Werner, F., Read, W. G., Park, M., Fuller, R. A., and Ward, B. M.: Prolonged and Pervasive Perturbations in the Composition of the Southern Hemi-
430   sphere Midlatitude Lower Stratosphere From the Australian New Year's Fires, Geophysical Research Letters, 49, e2021GL096 270, https://doi.org/10.1029/2021GL096270, 2022.

Saponaro, G., Kolmonen, P., Karhunen, J., Tamminen, J., and de Leeuw, G.: A neural network algorithm for cloud fraction estimation using NASA-Aura OMI VIS radiance measurements, Atmospheric Measurement Techniques, 6, 2301–2309, https://doi.org/10.5194/amt-6-2301-2013, 2013.

435 Schultz, M. G., Betancourt, C., Gong, B., Kleinert, F., Langguth, M., Leufen, L. H., Mozaffari, A., and Stadtler, S.: Can deep learning beat numerical weather prediction?, Phil. Trans. R. Soc. A., 379, https://doi.org/10.1098/rsta.2020.0097, 2021.

Schwartz, M. J., Read, W. G., Santee, M. L., Livesey, N. J., Froidevaux, L., Lambert, A., and Manney, G. L.: Convectively injected water vapor in the North American summer lowermost stratosphere, Geophysical Research Letters, 40, 2316–2321, https://doi.org/10.1002/grl.50421, 2013.

440 Schwartz, M. J., Santee, M. L., Pumphrey, H. C., Manney, G. L., Lambert, A., Livesey, N. J., Millán, L., Neu, J. L., Read, W. G., and Werner, F.: Australian New Year's PyroCb Impact on Stratospheric Composition, Geophysical Research Letters, 47, e2020GL090 831, https://doi.org/10.1029/2020GL090831, 2020.

Strahan, S. E. and Douglass, A. R.: Decline in Antarctic Ozone Depletion and Lower Stratospheric Chlorine Determined From Aura Microwave Limb Sounder Observations, Geophysical Research Letters, 45, 382–390, https://doi.org/https://doi.org/10.1002/2017GL074830,
445   2018.

Waters, J. W., Froidevaux, L., Harwood, R. S., Jarnot, R. F., Pickett, H. M., Read, W. G., Siegel, P. H., Cofield, R. E., Filipiak, M. J., Flower, D. A., Holden, J. R., Lau, G. K., Livesey, N. J., Manney, G. L., Pumphrey, H. C., Santee, M. L., Wu, D. L., Cuddy, D. T., Lay, R. R., Loo, M. S., Perun, V. S., Schwartz, M. J., Stek, P. C., Thurstans, R. P., Boyles, M. A., Chandra, K. M., Chavez, M. C., Gun-Shing Chen, Chudasama, B. V., Dodge, R., Fuller, R. A., Girard, M. A., Jiang, J. H., Yibo Jiang, Knosp, B. W., LaBelle, R. C., Lam, J. C., Lee, K. A.,
450   Miller, D., Oswald, J. E., Patel, N. C., Pukala, D. M., Quintero, O., Scaff, D. M., Van Snyder, W., Tope, M. C., Wagner, P. A., and Walch, M. J.: The Earth observing system microwave limb sounder (EOS MLS) on the aura Satellite, IEEE Transactions on Geoscience and Remote Sensing, 44, 1075–1092, https://doi.org/10.1109/TGRS.2006.873771, 2006.

Werner, F., Schwartz, M. J., Livesey, N. J., Read, W. G., and Santee, M. L.: Extreme Outliers in Lower Stratospheric Water Vapor Over North America Observed by MLS: Relation to Overshooting Convection Diagnosed From Colocated Aqua-MODIS Data, Geophysical Research
455   Letters, 47, e2020GL090 131, https://doi.org/10.1029/2020GL090131, 2020.

Werner, F., Livesey, N. J., Schwartz, M. J., Read, W. G., Santee, M. L., and Wind, G.: Improved cloud detection for the Aura Microwave Limb Sounder (MLS): training an artificial neural network on colocated MLS and Aqua MODIS data, Atmos. Meas. Tech., 14, 7749–7773, https://doi.org/10.5194/amt-14-7749-2021, 2021.